Note

Understanding enhanced charge storage of phosphorus-functionalized graphene in aqueous acidic electrolytes

Gelines Moreno-Fernández [a], Juan Luis Gómez-Urbano [a,b], Marina Enterría [a], Rosalia Cid [a], Juan M. López del Amo [a], Roman Mysyk [a], Daniel Carriazo [a,c,*]

[a] Centre for Cooperative Research on Alternative Energies (CIC energiGUNE), Basque Research and Technology Alliance (BRTA), Alava Technology Park, Albert Einstein 48, 01510 Vitoria-Gasteiz, Spain
[b] University of the Basque Country (UPV/EHU), 48940 Leioa, Spain
[c] IKERBASQUE, Basque Foundation for Science, 48013 Bilbao, Spain

ABSTRACT

The mechanisms behind enhanced charge storage of P-functionalized carbons are unraveled for the first time using non-porous graphene oxide treated with phosphoric acid and annealed at either 400 or 800 °C. The electrochemical study in 1 M H_2SO_4 reveals that phosphorus groups boost charge storage and electrochemical stability, with more effect for the higher annealing temperature. Annealing at 800 °C also leads to the material withstanding 60,000 charge-discharge cycles with no capacitance loss at 1.5 V. The improvement in the electrochemical performance is shown to be mainly governed by the change in surface chemistry comprehensively studied with NMR, FTIR and XPS characterization techniques. The collective analysis of electrochemical response and surface chemistry demonstrates that enhanced charge storage by phosphorus-functionalized graphene materials is made possible due to the following synergistic mechanisms: i) non-Faradaic charging; ii) nascent hydrogen storage in the interlayer; iii) benzoquinone-to-hydroquinone redox processes; iv) phosphate-to-phosphonate like transformation. From the practical perspective, the stored charge can be boosted due to the higher capacitance upon prior electrochemical activation in the vicinity of oxygen evolution potential and the wider usable electrochemical window enabled by phosphorus-related groups.

1. Introduction

Supercapacitors are energy storage devices filling the gap between dielectric capacitors and batteries in terms of power and energy density. The energy is physically stored at the electrode-electrolyte interface by the formation of an electric double layer (EDL) or by fast redox reactions on the electrode surface (pseudo-capacitance) virtually mimicking the electrochemical signature of an EDL. Consequently, the charge and discharge can proceed very quickly ensuring high power densities and long cycling stability [1–3]. Nevertheless, the low energy density stored, compared with that of batteries, calls for future research in new electrode materials and electrolytes.

In the last decade, graphene has emerged as a promising candidate to replace activated carbons in supercapacitors due to its large theoretical specific surface area (2630 m^2g^{-1}), outstanding electronic properties and superior mechanical strength [4–6]. However, bulk graphene and related materials (GRMs) tend to restack due to strong cooperative interlayer Van der Waals interactions, detrimentally to specific surface area. Apart from it, large-scale production of ideal monolayer graphene is still challenging due to the lack of cost-effective processing methods. For this reason, graphene oxide (GO) and derived materials, which can be easily obtained in large quantities by Hummers' method, have been majorly employed by the scientific community as a more viable alternative. In contrast with graphene, GO presents structural defects and a large amount of oxygen functional groups, which negatively affect the promising features of this material. Nevertheless, thanks to the rich chemistry of hydroxyl, carboxyl, and epoxy groups, the properties of GO can be tuned through the covalent attachment of functional groups to its surface. Furthermore, electronic properties can be further improved by the reduction of GO to rGO via thermal or chemical treatment. Heteroatom functionalization has been demonstrated to be a powerful method for enhancing the electrochemical

---

performance of GRMs, which does not interfere with large-scale production since GO can be used as the starting material. In fact, nitrogen (N), sulfur (S), boron (B) and oxygen (O) functionalization has been extensively demonstrated to enhance capacitive performance due to the improved electronic properties, fast redox reactions and better electrode wetting [7–10].

More specifically, the introduction of phosphorus heteroatoms can lead to improved charge storage due to the additional pseudocapacitive component alongside the electric double layer. Phosphorus also shows electron-donor characteristics and enhances the carrier density, i.e. an exceptionally high electrical conductivity [11]. Moreover, P-functionalization has been demonstrated to extend the practical potential window in aqueous electrolytes above the theoretical stability range of water (1.23 V). This fact was firstly demonstrated by Hulicova et al. in 2009 [12] who reported on P-rich carbons with a stable operation above 1.3 V. The effect of P-functionalization on the stability window was further corroborated by other research groups, concluding on a stable operation potential window of 1.4 and even 1.5 V in H_2SO_4 [13–17]. All those phenomena enabled supercapacitor energy densities as high as 44 and 59 Wh Kg^{-1} for P-functionalized carbons in aqueous (H_2SO_4) electrolytes, accompanied with stable cycle life and rate response [18,19]. Nevertheless, the mechanisms behind this behavior have not been yet clarified. Some studies suggest enhanced electro-oxidation resistance of the carbon-based electrode induced by phosphorus groups [20,21], others hypothesize the blocking of active sites of oxidation-susceptible functionalities [22,23], and also reversible hydrogen storage [24].

In this paper, we aim at shedding more light on the synergistic mechanisms behind the electrochemical performance of phosphorus-functionalized materials. To this end, the chemical state of phosphorus surface groups on graphene-based materials was varied by treating GO impregnated in phosphoric acid at two different temperatures (400 and 800 °C). The role played by temperature in the microstructure and surface chemistry was explored and correlated with the electrochemical performance. The improved charge storage observed for the electrode functionalized at high-temperature has been carefully studied in order to understand the origin of the wider potential window, higher specific capacitance and fast rate response as well as the excellent cycling stability of cells operating at 1.5 V in aqueous 1 M H_2SO_4.

2. Experimental

2.1. Sample preparation

Phosphorus-functionalized graphene oxide was obtained by adding 200 μL of phosphoric acid to 50 ml of commercial graphene oxide (GO) (4 mg mL^{-1}, Graphenea) and stirring until homogenization. Then, the mixture was transferred into a closed recipient to an oven at 80 °C for 18 h to succeed the hydrothermal condensation. A subsequent freeze/freeze-drying process was carried out for 3 days to obtain the dry material (hereafter denoted as GO-P). In order to study the modification of the surface chemistry with the temperature, GO-P was thermally treated at 400 and 800 °C for 1 h in a tubular oven under dynamic argon flow (70 mL min^{-1}). As-obtained samples were denoted as GO-P-R400 and GO-P-R800, respectively.

For the sake of comparison, reduced graphene oxide samples (GO-R400 and GO-R800) were also prepared following the same route but in the absence of phosphoric acid.

2.2. Physicochemical characterization

The morphological characterization of GRMs was performed by Scanning Electron Microscopy (SEM) using a FEI Quanta250

microscope operating at 30 kV. Nitrogen adsorption-desorption isotherms at −196 °C of the GRMs in powder and the processed electrodes were measured using ASAP2460 instrument from Micromeritics. Prior to the analysis, GRM powders or electrodes were outgassed under vacuum at 250 °C for 12 h or 110 °C for 16 h, respectively. The specific surface area (S_{BET}) was calculated according to the Brunauer–Emmett–Teller (BET) method and 2D-NLDFT from the nitrogen isotherms. The ultramicroporosity of the samples was studied by CO_2 adsorption isotherms at 0 °C using ASAP2020 adsorption analyzers (Micromeritics). The ultramicropore surface area (S_{DR}) was calculated by applying the Dubinin-Radushkevich (DR) method to the CO_2 isotherms in the relative pressure range of DR graph linearity between 10^{-5} and 0.03. Thermogravimetric analysis was performed to study thermal stability using a TG209 F1 Libra equipment in air atmosphere with a heating rate of 5 °C min^{-1} from RT to 900 °C. Solid state NMR experiments were performed using a WB500Hz spectrometer equipped with a 2.5 mm magic angle spinning (MAS) probe. The MAS frequency used in all cases was set to 20 kHz and experiments were collected at room temperature. ^{31}P NMR spectra were acquired using single pulse experiments with a recycling delay of 6 s and a $\pi/2$ excitation pulse of 2.5 μs. ^{13}C NMR spectra were acquired using rotor synchronized echo experiments and a recycling delay of 15 s. Attenuated total reflection Fourier transform infrared (ATR-FTIR) spectrophotometry (Spectrum 400 DTGS PERKIN-ELMER) was performed to analyze the chemical bonds of the samples. Prior to the analysis the sample chamber was flushed with Ar gas for several hours. Spectra were measured using a wave number between 400 and 4500 cm^{-1}. X-ray Photoelectron Spectra were recorded using a Phoibos 150 XPS spectrometer (SPECS Surface Nano Analysis) installed in a UHV chamber with a base pressure of 10^{-10} mbar.

2.3. Electrode preparation, cell assembling and electrochemical characterization

The graphene-based powder was mixed with Super P C-65 (Imerys Graphite & Carbon) conductive carbon and polytetrafluoroethylene (PTFE) binder in a mass ratio of 85:10:5 in the presence of ethanol. Circle-shaped electrodes of 10 mm in diameter were prepared by applying a pressure of 0.5 Ton for 1 min. Electrode masses of ca. 7, 8, 13 and 10 mg and thickness of ca. 196, 431, 152 and 317 μm were measured for GO-R400, GO-R800, GO-P-R400 and GO-P-R800, respectively. The apparent density of the processed electrodes was calculated by weighing and measuring their dimensions upon drying at 120 °C for 12 h in vacuum.

The electrochemical performance in the aqueous electrolyte (1 M H_2SO_4) was studied in a three-electrode Swagelok-type T-cell. As-prepared graphene-based electrodes were used as the working electrode, while oversized Norit and Hg/Hg_2SO_4 (K_2SO_4 sat.) as the counter and reference electrodes, respectively. Two stainless steel rods were used as the current collectors. Electrochemical impedance spectroscopy (EIS) (signal amplitude 10 mV, frequency range 1 MHz-10 mHz), cyclic voltammetry (CV) (at the scan rates of 5–100 mVs^{-1}) and galvanostatic charge-discharge (GV) measurements (at the current densities of 0.2–40 mA g^{-1}) were performed using a multichannel VMP3 generator from Biologic.

The specific capacitance ($F\,g^{-1}$) was calculated from the CV experiments according to the formula:

$$C_s = \frac{\int i \cdot dE}{V_{scan\,rate} \cdot \Delta E \cdot m_{act}}$$

and from the discharge galvanostatic plots at different current densities, following the equation:

$$C_s = \frac{(I \cdot t)}{(\Delta E \cdot m_{act})}$$

where i is the instant current, E is the instant working potential, I is the current density, t is the discharge time, ΔE is the
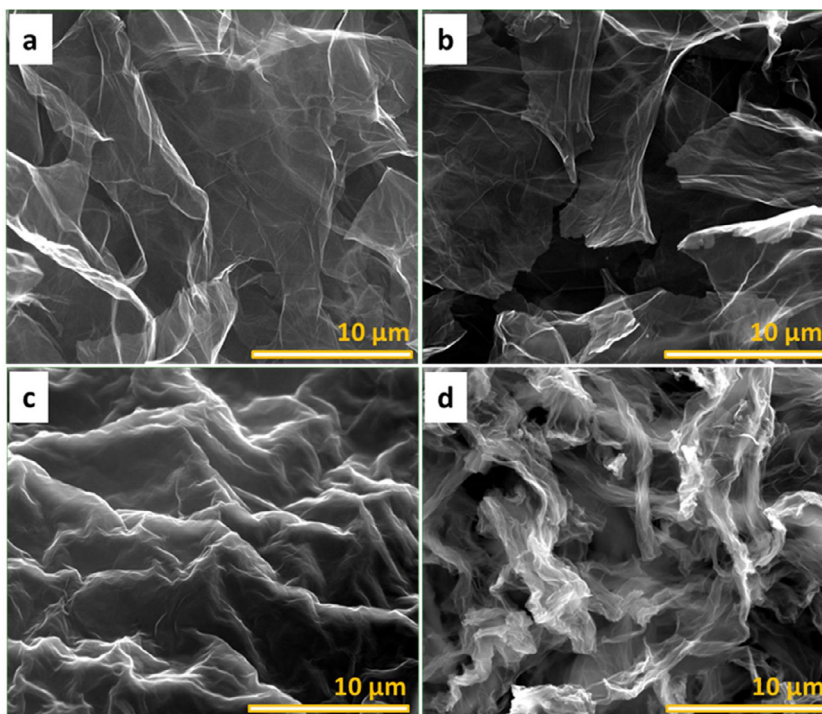
Fig. 1. SEM images of: (a) GO-R400, (b) GO-R800, (c) GO-P-R400 and (d) GO-P-R800.

working potential range once the total resistance drop is subtracted and m_{act} is the mass of active material in a single electrode. The same equation was applied for the electrode capacitance in the symmetric cells built to evaluate the energy and power densities by adopting electrode potential ΔE to be half the cell potential V.

Energy W (Wh kg^{-1}) and power P (W kg^{-1}) densities were calculated for symmetric two-electrode cells according to the following equations:

$$W = \frac{1}{3.6}\left(\frac{1}{8}C_s \cdot \left(V_{max}^2 - V_{min}^2\right)\right)$$

$$P = \frac{W}{t_d}$$

where V_{max} and V_{min} the maximum and the minimum of the cell potential in two electrode symmetric cells.

3. Results and discussion

The morphology and microstructure of the GRMs were evaluated by SEM imaging. As can be noted in Fig. 1, no significant morphological changes are observed between GO-R400 and GO-R800 samples (Fig. 1**a** and Fig. 1**b**, respectively), which maintain the pristine porous network of GO (**Figure S1**). By contrast, the phosphorus-containing samples show a more crumpled and wrinkled framework. Specifically, GO-P-R400 (Fig. 1**c**) graphene sheets seem to restack, forming a dense agglomerate while GO-P-R800 (Fig. 1**d**) shows a slightly less aggregated structure due to the release of some functional groups as gas evolved at the higher temperature. The surface elemental composition was evaluated by Energy-dispersive X-ray spectrometry (EDX) (Table 1). It seems that both O and P content decreases upon rising temperature.

Solid state NMR experiments were performed in order to characterize the nature of the functional groups in the as-synthetized and thermally treated graphene-based materials. Fig. 2**a** shows the ^{13}C NMR spectra of both carbon precursors GO and GO-P evidencing that the surface of pristine GO is rich in alcoholic and epoxylike groups (C−OH and C−O-C). Main signals in the spectra and cor-

responding functional groups are in good agreement with previously reported publications for GRMs [25,26]. The absence of the signals assigned to C−O bonds in the spectra of GO-P sample reveals that the addition of phosphoric acid to graphene oxide results in the depletion of these oxygen functionalities from the surface of the material [22]. The ^{31}P solid state NMR spectrum of the GO-P sample is shown in Fig. 2**b** together with the spectra obtained for the thermally treated samples (GO-P-R400 and GO-P-R800). The ^{31}P NMR spectrum of GO-P is characterized by a broad signal whereas the much sharper signals of the GO-P-R400 and GO-P-R800 indicate the presence of more defined and homogeneous surface chemistry. The area of the ^{31}P NMR signals is also drastically reduced upon temperature treatment (**Figure S3),** therefore indicating that elemental phosphoric acid and a large phosphate population weakly bound to the material surface is removed by the temperature treatment and that the remaining P-based functional groups are more homogeneous in nature. The dominant signal around 0 ppm in Fig. 2**b** can be ascribed to elemental phosphoric acid and phosphate-like functional groups, i.e., phosphorus bound to four oxygen atoms with a C−O-P = O bond structure [27–29]. This signal is observed in the spectra of the three materials regardless of the annealing temperature. The second peak at 30 ppm defined in the carbon treated at 800 °C (GO-P-R800) can be assigned to phosphonate groups, i.e., groups with a C-P = O bond structure [30].

FTIR characterization (Fig. 3) further confirms the phosphorus groups assigned in each sample by NMR. The characteristic absorption peaks observed for the samples annealed at 400 °C are shown in Fig. 3**a**. The peak at 3545 cm^{-1} is attributed to the stretching vibration of O−H or the trapped water [31–33], evidencing the highly hygroscopic behavior of GO-P-R400 compared to GO-R400. The peaks of GO-R400 registered at 1740, 1580 and 1209 cm^{-1} correspond to $C = O$, $C = C$ and C−O-C stretching vibration, respectively [32,33]. Upon functionalization (GO-P-R400) $C = O$ stretching vibration is shifted to 1800 cm^{-1} due to the lower involvement of carboxylic acids in hydrogen bonding [33]. New peaks appearing at 588, 950 and 1110 cm^{-1} correspond to in-plane deformation,
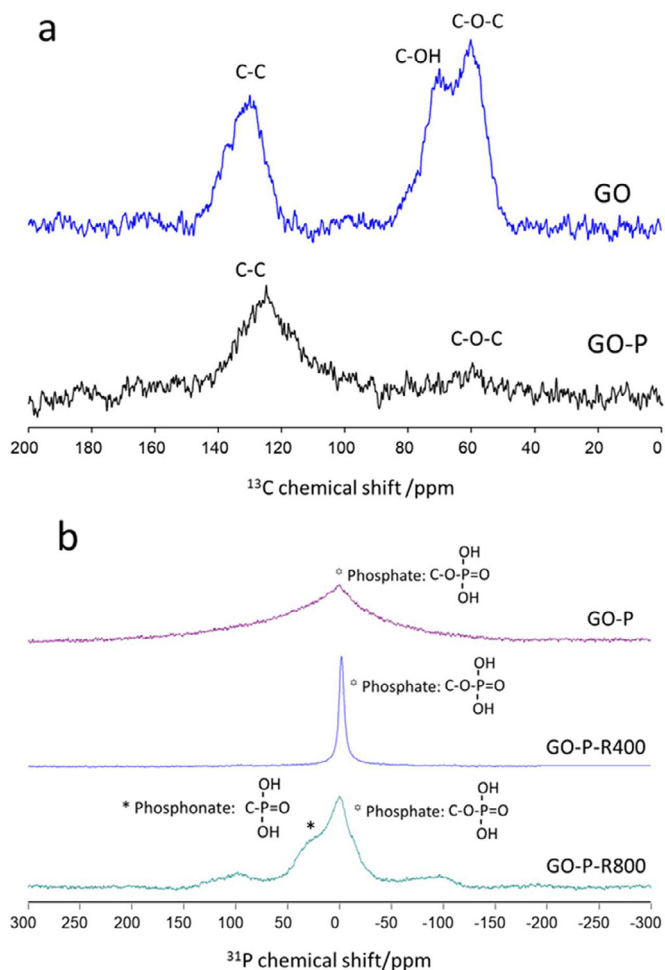
Table 1
Elemental composition obtained from EDX and XPS and textural parameters obtained from N_2 adsorption-desorption isotherms at -196 °C of the processed electrodes.

	EDX			XPS			N_2	
	C^a (%)	O^a (%)	P^a (%)	C^b (%)	O^b (%)	P^b (%)	S_{BET} (m^2g^{-1})	S_{DFT} (m^2g^{-1})
GO-R400	88	12	–	–	–	–	28	30
GO-R800	92	8	–	–	–	–	58	61
GO-P-R400	63	28	9	46	42	10	4	4
GO-P-R800	87	7	6	74	17	3	9	6

[a] Carbon, Oxygen and phosphorus content (at.%) obtained by EDX.
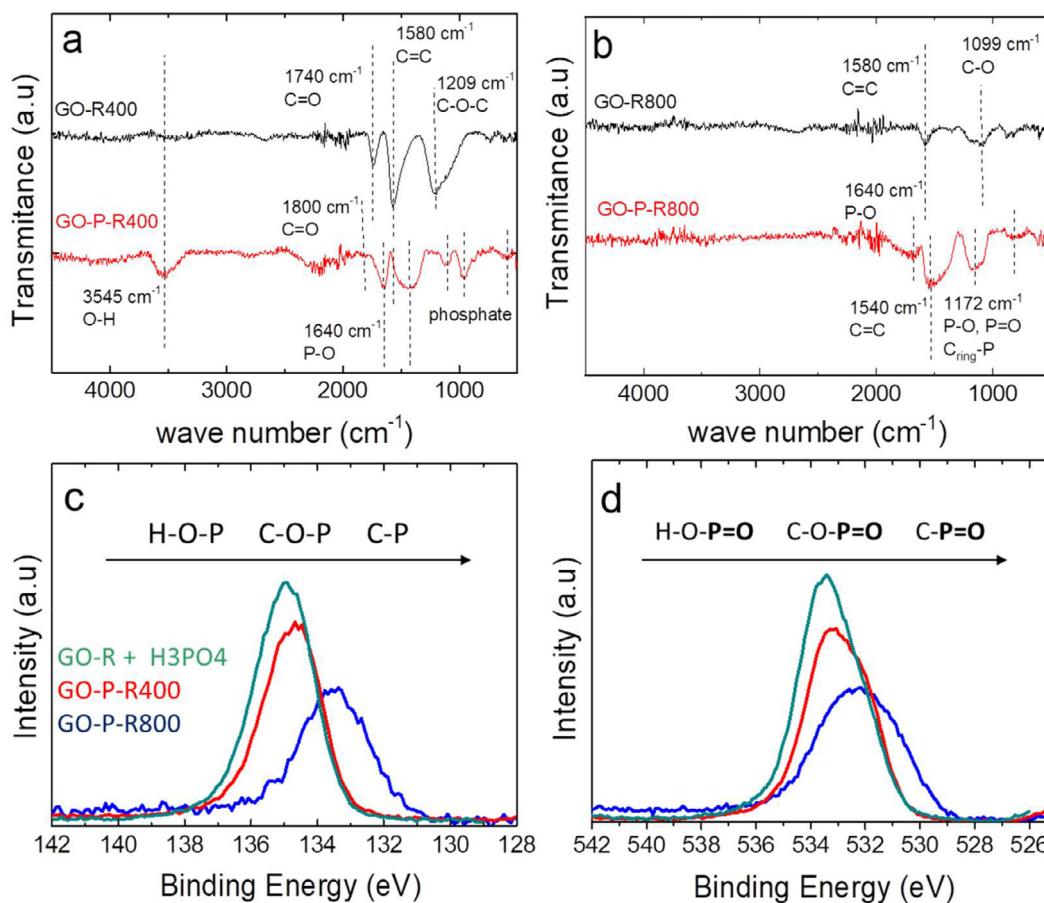[b] Carbon, Oxygen and Phosphorus surface content (at.%) obtained by XPS.

Fig. 2. ^{13}C Solid state NMR spectra of the pristine carbon precursors GO and GO-P (a) and ^{31}P Solid state NMR spectra of the noted P-functionalized graphene-based materials (b).

The XPS analysis of the functionalized materials (Fig. 3**c** and **d**) confirms the presence of phosphorus (Table 1) and suggests the chemical state of phosphorus groups in both GO-P-R400 and GO-P-R800. For a better assignment of the different type of bonding in phosphorus functionalities, GO-R400 was impregnated with H_3PO_4 and measured in the same conditions as the reference. A careful calibration of the spectra was carried out by setting $C = C$ at 284.4 eV after C1s deconvolution applying the method of Kovtun et al. [34], as detailed in the SI file (**Figure S4a**). The signal at ~135.0 eV, observed in the P2p core level spectra (Fig. 3**c**), was ascribed to the H−O−P groups in free phosphoric acid on the surface of the reference material. The centroid of the P2p signal shifts gradually to lower binding energies as the temperature of the treatment increases [35]. Such displacement reveals the presence of phosphorus species covalently bonded to the carbon atoms in graphene, either by oxygen bridges (C−O−P, phosphates) or via direct bonding (C-P, phosphonates). The presence of free phosphates on the surface of GO-P-R400 sample is confirmed by a $P2p_{3/2}$ signal centered at ~134.6 eV, while the decrease in the binding energy to ~133.4 eV in GO-P-R800 reveals the formation of C−O−P type phosphates linked to carbon atoms [35,36]. This trend is confirmed by further analysis of the O1s region (Fig. 3**d**) where the centroid observed in the reference sample at ~ 533.5 eV is displaced to 532.2 eV for GO-R800 material. Hence, the contribution of $P = O$ bonds to the XPS signal envelope shifts to lower binding energies as the chemical oxidation of phosphorus decreases.

Textural properties of the synthetized GRMs were studied by N_2 adsorption/desorption at -196 °C and CO_2 adsorption at 0 °C. The nitrogen adsorption isotherms (**Figure S5a)** of GO-R400 and GO-R800 correspond to a mixture of II and IV type [37]. A noticeable reduction in the adsorption capacity of N_2 is detected after P-functionalization for GO-P-R400 and GO-P-R800, which indicates a less developed porosity, likely resulting from micropore clogging with P-functional groups and the restacking of graphene sheets [24]. The ultramicroporosity was studied by CO_2 adsorption (**Figure S5b**) to further confirm this hypothesis. Thus, the lower CO_2 uptake for GO-P-R800 compared to GO-R800 supports the latter assumption. After electrode processing (Fig. 4**a**) the volume of adsorbed N_2 is reduced due to the higher restacking of graphene sheets upon pressing, and also the collapse of some pores with the PTFE binder. The specific surface area (SSA) increases with temperature and the absence of P-functionalization, but is in all cases low (Table 1), suggesting that all the materials are mostly non-porous. The cumulative pore volume (Fig. 4**b**) reveals a continuous pore size distribution with pores mainly in the mesopore range and is broader for the non-functionalized electrodes. Nevertheless, these values should just be taken as reference because they can significantly differ from the electrochemically active surface for GRMs [38]. Specifically, polar aqueous electrolytes can seep into the interlayer of rGO-derived graphene functionalized with polar moieties, making the surface of functionalized graphene layers available for electrochemical charge storage by both non-Faradaic and Faradaic

symmetric bridge and asymmetric bridge vibrations of phosphate groups, respectively. The band at 1417 cm^{-1} may also be related to phosphoric acid groups and the band at 1640 cm^{-1} corresponds to the P-O bond [31,33]. Fig. 3**b** reveals the characteristic absorption peaks observed for the samples annealed at 800 °C. The stretching vibration of the $C = O$ bond in GO-R800 disappears, confirming the successful reduction process. The peaks at 1099 and 1580 cm^{-1} can be assigned to the stretching vibration of C−O and $C = C$, respectively [32]. The spectrum of GO-P-R800 reveals that the treatment with phosphorus at higher temperatures shifts the $C = C$ vibration to 1540 cm^{-1} and that P-O, C_{ring}-P and $P = O$ overlap in a broad peak centered at 1172 cm^{-1} [32,33].

Fig. 3. FTIR spectra GO-R400, GO-P-R400 (a) and GO-R800, GO-P-R800 (b). P2p (c) and O1S (d) high-resolution XPS spectra for GO-P-R400, GO-P-R800 and reduced graphene oxide impregnated with phosphoric acid (used as reference). (For interpretation of the references to colour in this figure legend, the reader is referred to the web version of this article.)
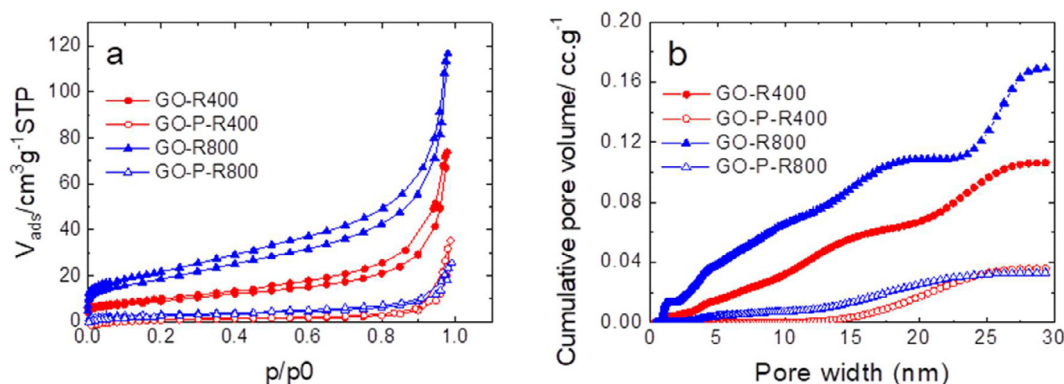

Fig. 4. (a) Nitrogen Adsorption/desorption isotherms at −196 °C for the processed electrodes and (b) cumulative pore volume derived by 2D-NLDFT.

mechanisms. However, this surface is inaccessible for detection in the vacuum-dried materials used in gas adsorption analysis.

The apparent density measured for the electrodes made out of GO-R400, GO-R800, GO-P-R400 and GO-P-R800 was 0.46, 0.24, 1.09 and 0.40 g cm^{-3}, respectively. From these values, it can be stated that the apparent density decreases on increasing the temperature due to the removal of oxygen functionalities and increases upon the addition of phosphorus due to the higher weight of this element. An interesting feature is that the density of the P-functionalized samples is around twice that of the non-functionalized; 0.53 vs 1.07 g cm^{-3} for carbons reduced at 400 °C and 0.21 vs 0.47 g cm^{-3} for those reduced at 800 °C. Furthermore,

the density of GO-P-R400 (1.07 g cm^{-3}) is higher than that typically reported for activated carbons (0.5–0.7 g cm^{-3}) [39,40].

The electrochemical performance of these materials was firstly evaluated in the three-electrode cell configuration using 1 M H_2SO_4 as aqueous electrolyte. Impedance spectroscopy (**Figure S6**) shows an almost ideal capacitive behavior for all the samples. The close-up of the high-frequency region (**Figure S6-inset**) points to the low ESR values for the four materials and the absence of any semicircle, which is commonly associated with an insulating layer on the current collectors [41,42]. The no-semicircle spectra also indicate no corrosion issues with the selected current collectors in the aggressive acidic electrolyte. At the medium-to-low frequency
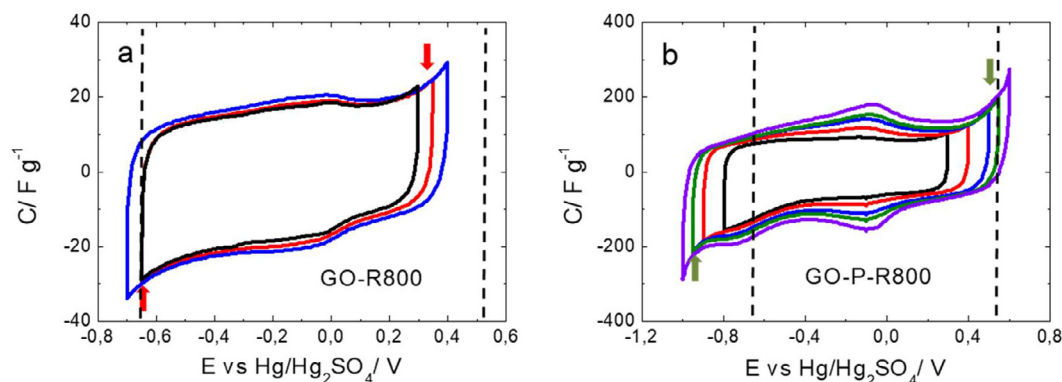
Fig. 5. Determination of the stability voltage window (ΔE) from cyclic voltammetry at 5 mV s^{-1} for: (a) GO-R800 and (b) GO-P-R800. The dashed vertical lines correspond to the thermodynamic potentials of water splitting.

region, the samples reduced at 400 °C show a less vertical capacitive line than those reduced at 800 °C. This is mainly due to the higher amount of poorly conductive surface groups anchored to the graphene layers at the lower annealing temperature, which makes capacitance more disperse because of the less homogeneous electrode. Apart from it, for both temperatures the corresponding P-functionalized material displays more vertical lines, meaning better capacitive features.

Cyclic voltammetry was first conducted to establish the operating voltage window for each graphene-based electrode using previously reported criteria [43]. The thus-obtained voltammograms were analyzed using the E-pH Pourbaix diagram of water with respect to the thermodynamic values for oxygen and dihydrogen evolution in 1 M H_2SO_4 [44] (Fig. 5).

GO-R800 (Fig. 5**a**) displays a noticeable increase in the positive current for potentials above 0.35 V and a decrease in the negative current for potentials below −0.65 V (red voltammogram and red arrows), which indicates oxygen and dihydrogen evolution, respectively. The stability potential window of GO-R800 was therefore limited to −0.65 to 0.35 V (i.e. $\Delta E_{GO-R800}$ =1.0 V) which is below the thermodynamic stability of water (1.23 V). Since the experimental and thermodynamic values for dihydrogen evolution potential in GO-R800 coincide (Fig. 5**a**), the narrow potential range of this electrode is ascribed to its high reactivity at lower potential than thermodynamic oxygen evolution. By contrast, the stability potential window is extended to $\Delta E_{GO-P-R800}$ =1.5 V for the phosphorus containing GO-P-R800 sample (Fig. 5**b**), since the experimental negative decomposition limit is shifted to −0.95 V, well below the thermodynamic dihydrogen evolution potential, while the positive decomposition limit is displaced to 0.55 V (green voltammogram and green arrows).

A close examination of Fig. 5**b** reveals that the shape of CV profiles varies significantly depending on the limits of the potential window. Specifically, the potential window between −0.8 and 0.25 V (black voltammogram) leads to the redox peak at −0.1 V being barely noticeable even though (pseudo)capacitive storage is quite important. In contrast, when the potential excursion is extended between −0.95 and 0.55 V (green voltammogram), the redox peaks at −0.1 V become more prominent and the capacitance is boosted from 72 F g^{-1} to 128 F g^{-1}. In addition, the widening of the operational window reveals an additional redox peak (ca. −0.9 V) farther beyond the thermodynamic dihydrogen evolution potential (−0.65 V). Similar results were obtained for the samples reduced at 400 °C ($\Delta E_{GO-R400}$ =1.2 V and $\Delta E_{GO-P-R400}$ =1.5 V). However, surprisingly the additional peak at −0.9 V is not observed for GO-P-R400 (**Figure S7**).

To better understand the electrochemical response of GO-P-R800, a separate experiment (Fig. 6) was conducted where the
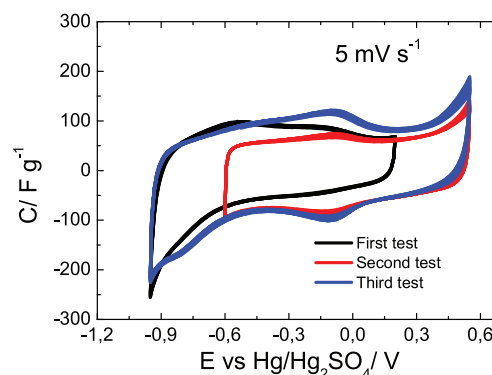
Fig. 6. Cyclic voltammograms recorded at 5 mV s^{-1} in various voltage ranges for GO-P-R800.

freshly made working electrode was first subjected to cycling between −0.95 V and 0.2 V, subsequently between −0.6 V and 0.55 V, and finally between −0.95 V and 0.55 V. The first cycling (black curve) was deliberately limited to 0.2 V so as to prevent any oxidation of the material and/or oxygen evolution. Negative polarization reveals a wide wave for potentials below −0.6 V with a subsequent positive polarization hump at about −0.5 V. The curve obtained in the second cycling (red curve) yields an almost square shape with a slight redox activity around −0.1 V that alludes to a transformation akin to that of benzoquinone to hydroquinone[22,43,44]. The widening of the working potential from −0.95 to 0.55 V (blue curve) not only promotes an intense redox activity of quinones (−0.1 V) but also leads to an additional redox peak at −0.90 V. The wider electrochemical window is typically displayed by ultramicroporous carbons where the weak chemisorption of atomic (nascent) hydrogen in small pores results in H_2 evolution overpotential [45]. By contrast, our work suggests this phenomenon to occur for GO-P-R800, which is non-porous prior to electrochemical tests. In addition to nascent hydrogen storage, the negative shift in dihydrogen evolution can, at least partially, be related to the involvement of protons in the conversion of phosphates to phosphonates according to:

$$-CH_2PO_4 + 2H^+ + 2e^- \rightleftharpoons -CH_2PO_3 + H_2O$$
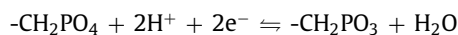
This assumption is based on the redox peak at −0.9 V in the CVs of GO-P-R800 which coincides with the standard reduction potential of the analogous inorganic reaction $H_3PO_4 + 2H^+ + 2e \rightleftharpoons H_3PO_3 + H_2O$ (E^0= −0.28 V or −0.93 V vs Hg/Hg$_2$SO$_4$[46], See Supporting Information). It is also possible that the conversion to phosphonates is promoted at more positive potentials than
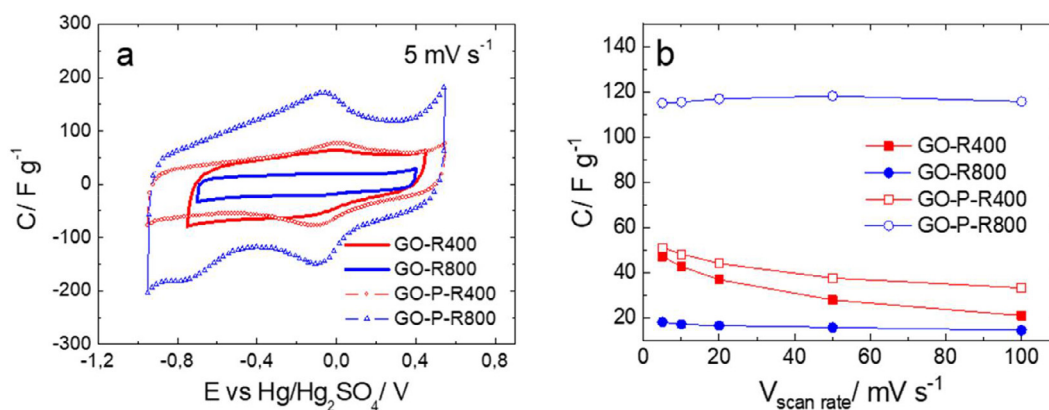
Fig. 7. (a) Cyclic voltammograms recorded at 5 mV s^{-1} showing gravimetric specific capacitance and (b) dependence of the gravimetric specific capacitance on the scan rate.

Table 2

Working potential window (ΔE), gravimetric capacitance (C), volumetric capacitance (C_V), capacitance retention at 100 mV s^{-1} ($C_{Retention}$) and capacitance retention after 60,000 cycles at 10 A g^{-1} ($C_{Cycling}$).

|	ΔE (V)	C (F g^{-1})	C_v (F cm^{-3})	$C_{Retention}$ (%)	$C_{Cycling}$ (%)
GO-R400	1.2	47	21	45	–
GO-R800	1.0	17	4	83	–
GO-P-R400	1.5	51	56	65	121
GO-P-R800	1.5	115	46	100	105

predicted (-0.93 V) using the above inorganic reaction of H_3PO_4 as a reference. Thus, the not mutually exclusive mechanisms for dihydrogen are envisioned to be nascent hydrogen storage (< -0.65 V) and conversion of phosphates to phosphonates (< -0.93 V). In practical terms, **Figs. 5** and **6** reveal that GO-P-R800 in 1 M H_2SO_4 can be more useful than GO-R800 for energy storage because of its higher capacitance/pseudocapacitance and the wider electrochemical stability window.

The comparison of the voltammograms of all the GRMs (Fig. 7**a**) points out that the phosphorus-containing samples display a wider stability potential window while the dramatic enhancement of specific capacitance occurs for GO-P-R800. For the phosphorus-free samples, the higher specific capacitance of GO-R400 (47 F g^{-1}) vs GO-R800 (17 F g^{-1}) can be ascribed to its higher concentration of reversible redox-active quinone/ hydroquinone groups[43]. These redox peaks became intensified for GO-P-R400, although similar gravimetric capacitance to GO-R400 (about ~50 F g^{-1}) is found at low scan rates. Nevertheless, GO-P-R400 clearly overperforms GO-R400 at higher scan rates (Fig. 7**b** and Table 2), mostly due to the improved electronic conductivity provided by phosphate groups. For the samples reduced at 800 °C, the gravimetric capacitance is 7 times boosted from pristine GO-R800 sample (17 F g^{-1}) to the P-functionalized GO-P-R800 (115 F g^{-1}). Regarding both phosphorus-containing samples (GO-P-R400 and GO-P-R800), the higher reduction temperature leads to the higher gravimetric capacitance and better capacitance retention (Fig. 7**b**). It can be due to the depletion of oxygen functionalities and weakly bonded phosphate species at 800 °C and/or the appearance of phosphonate functionalities (Fig. 2**b, 3b, 3d**) with C-$P = O$ bonding that enhances electronic conductivity, wettability and also redox storage processes [36,47]. From the volumetric point of view (**Figure S8**), GO-P-R400 outperforms GO-P-R800 at low scan rates due to its higher apparent density. Nevertheless, the improved features of GO-P-R800 results in a better capacitance retention. In fact, the capacitance retention is 100% at 100 mV s^{-1}. To conclude, phosphorus functionalization clearly improves the usable potential window, specific capacitance and capacitance retention. Besides, low surface

area measured (Table 1) corresponds to an anomalously high specific capacitance (Table 2) if compared to other carbon materials with similar SSA. This phenomenon was previously reported for GO materials [38].

In order to study the cycling stability of the phosphorus-functionalized samples (GO-P-R400 and GO-P-R800) 60,000 charge/discharge cycles were performed at 10 A g^{-1}. Fig. 8**a** shows an exceptional cycling stability for both samples even at the wide potential window of 1.5 V. No sign of degradation was observed even after 60,000 cycles, which can be related to the stability and/or reversibility of the phosphate functional groups present in the samples. Moreover, a little increase in capacitance is noticed (Fig. 8**b**), maybe related to the activation of the samples upon cycling. This capacitance increase is higher for GO-P-R400, likely due to the higher content of blocking functional groups such as weakly bonded phosphates and phosphoric acid that are irreversibly swept away in the initial cycles. This enables better electrolyte access to the bulk material, increasing the electrochemically active surface.

Post-mortem solid-state NMR experiments were conducted in order to study changes in the surface chemistry of both GO-P-R400 and GO-P-R800 upon cycling. Fig. 9 illustrates the differences in the phosphorus surface groups (^{31}P NMR signals) before (pristine, blue line) and after 60,000 charge/discharge cycles (cycled, green line). As can be seen from Fig. 9**a**, the total intensity of the signal ascribed to surface phosphate groups is strongly reduced for GO-P-R400 upon cycling (~10%). As well, no shift is observed on the ^{31}P NMR signal, suggesting that the chemical state of the species after cycling GO-P-R400 electrode remains as C–O–P like phosphates. In contrast, the spectrum for GO-P-R800 confirms the existence of chemical stable phosphorus-containing groups as the total intensity of the ^{31}P signal barely changes after charge/discharge cycling (Fig. 9**b**). Interestingly, a slight change in the chemical state of the phosphorus functionalities is observed, the content of phosphate groups decreased from 74% to 62% and phosphonate functionalities increased from 26% to 38% (as calculated from the total ^{31}P intensity). A separate NMR analysis of the GO-P-R800 electrode after the initial voltammetry scan (Fig. 5**b**, -1 to 0.6 V) demonstrates that the loss of the most weakly bonded phosphate groups takes place on extending the potential window and is not a consequence of cycling (**Figure S9**). The XPS analysis of P-functionalized electrodes confirmed the proposed chemical evolution of phosphorus throughout cycling on the electrodes surface. The intensity of the P2p signal for GO-P-R400 electrode is strongly reduced after cycling, in contrast to GO-P-R800 (compare **Figs. 9c** and **d**). The shift of the peak centroid in GO-P-R400 to lower binding energies reveals the enlarged proportion of phosphates linked to the graphene structure. It is hypothesized that, during cy-
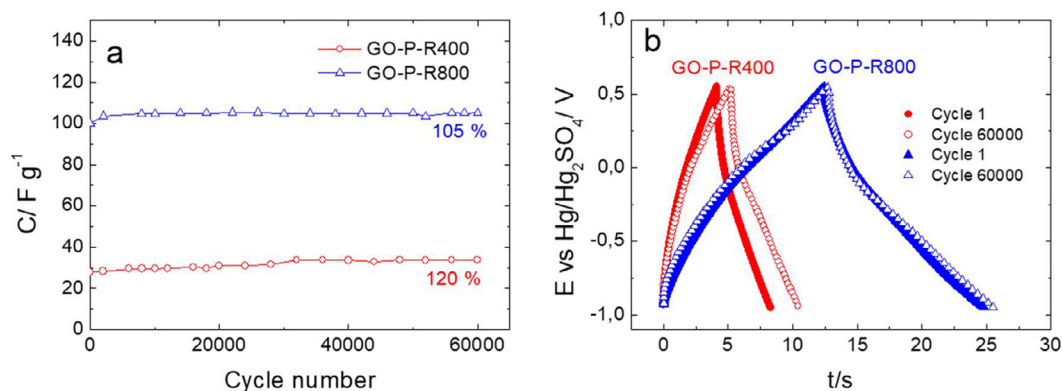
Fig. 8. Cycling tests at a current density of 10 A g^{-1} and potential window of 1.5 V for P-functionalized samples: (a) Gravimetric capacitance vs cycle number and (b) comparison of galvanostatic charge/discharge profiles for cycle 1 and cycle 60,000.
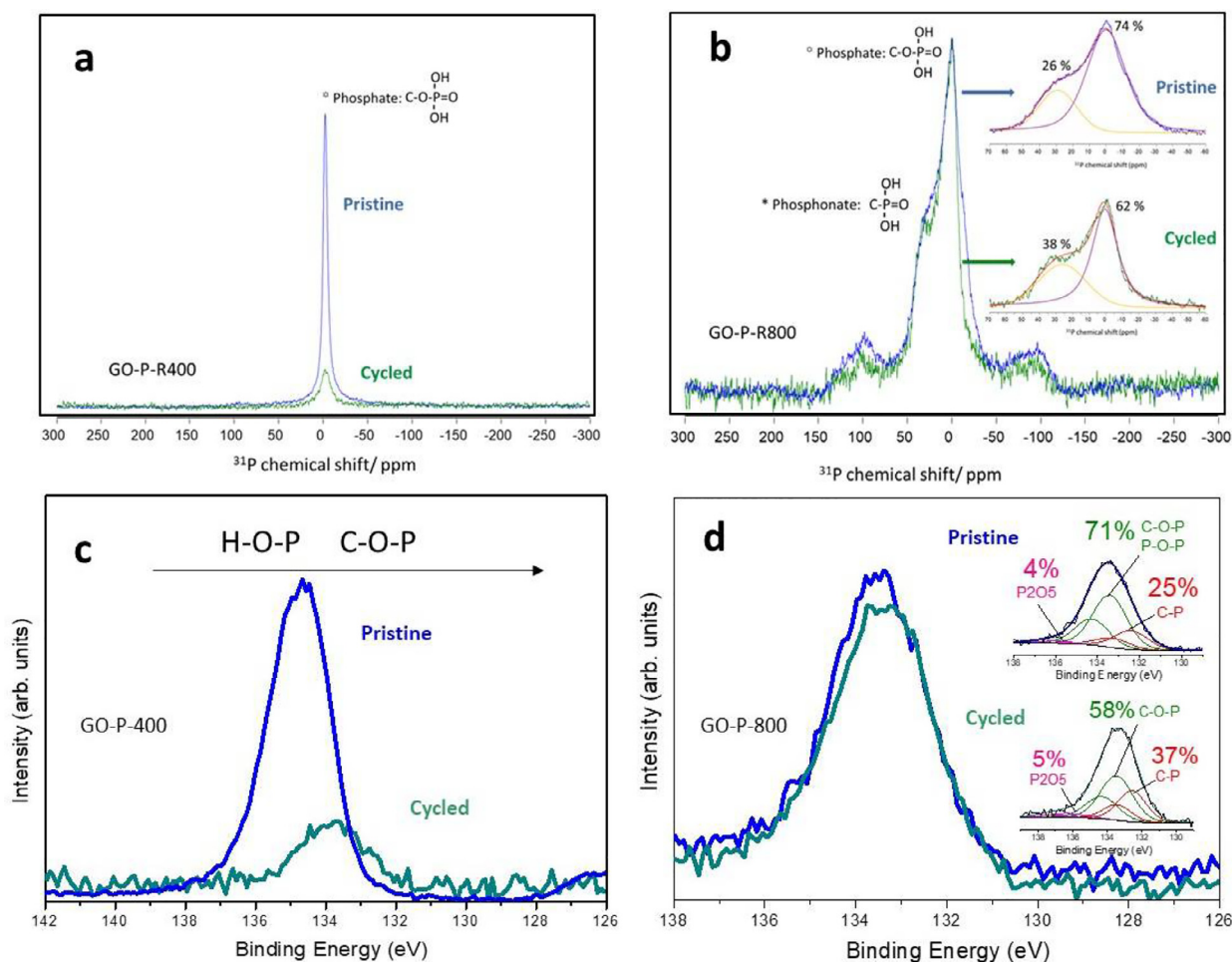
Fig. 9. ^{31}P Solid state NMR spectra of pristine (blue) and cycled (green) samples: (a) GO-P-R400 and (b) GO-P-R800. XPS high resolution P2p core-level spectra for pristine and cycled (c) GO-P-R400 and (d) GO-P-R800 electrodes. (For interpretation of the references to colour in this figure legend, the reader is referred to the web version of this article.)

cling, a large number of free molecules of phosphoric acid/phosphates/polyphosphates are dissolved in the acid electrolyte where only the phosphates bonded to the carbon atoms in the graphene sheets endure the cycling. Hence, the sensitivity of the XPS analysis for the C−O−P species increases after cycling as they were shielded by a thick layer of unbounded and labile phosphate species deposited onto the GO-P-R400 surface. An in-depth inspection of the surface chemistry by deconvolution of the P2p spectra for the cycled GO-P-R800 electrode (Fig. 9**d**,

green line) confirms a larger proportion of phosphonate species in detriment to phosphates as compared with the uncycled material (Fig. 9**d,** blue line). Thus, the atomic proportion of C-P bonds increases from 25 to 37% upon cycling while the relative percentage of C−O−P functionalities decreases from 71 to 58%. These observations are strengthened by deconvolution of the O1s spectra (**Figure S3b**) where the signal ascribed to $P = O$ bonding in phosphates shifts to lower binding energies after cycling for both GO-P-R400 and GO-P-R800. In the case of GO-P-R400, the

contribution for *P = O* bonds belonging to phosphorus linked to terminal OH groups in free phosphates/polyphosphates shifts to that ascribed for phosphates linked to carbon atoms (C−O-P-O and C−O-*P = O*). In GO-P-R800 the relative contribution for both C-P-O and C-*P = O* bonding increases after cycling. From the comprehensive characterization conducted by different techniques, it can be concluded that the weaker phosphate bondings (C−O-P), mainly observed in the GO-P-R400 sample, are easily removed from the carbon substrate whereas phosphonates groups (C-*P = O*) are more resistant to electrochemical cycling. These results support the differences observed in the CV profiles for GO-P-R400 and GO-P-R800 (Fig. 5b and S7b). The population of stable phosphates stronger bonded to the graphenic matrix is larger for GO-P-R800 than for GO-P-R400 (Fig. 3c and 3d), and it seems that only phosphates strongly bonded can store nascent hydrogen and be converted to phosphonate species (redox peak at −0.9 V) since weaker bonded phosphates are released to the electrolyte upon cycling. Even considering that a small contribution of strongly bonded electrochemically active phosphates are present on the GO-P-R400 sample, its lower electronic conductivity could limit its redox activity at −0.9 V.

To compare the practical energy storage characteristics of GO-R800 and GO-P-R800, symmetric 2-electrode cells were assembled in the aqueous 1 M H_2SO_4 electrolyte and cycled at several current densities. The Ragone plot (**Figure S10a**) shows that the gravimetric energy delivered by the phosphorus-containing material at low power densities 8 Wh Kg^{-1} is sixteen times that of the pristine sample 0.5 Wh Kg^{-1}. At the higher power density of 6.6 kW Kg^{-1}, an energy density as high as 5 Wh Kg^{-1} is delivered by GO-P-R800 in contrast to 0.07 Wh Kg^{-1} delivered by GO-R800. The impact of phosphorus is even more pronounced for volumetric values (**Figure S10b**) since the energy density provided by the P-functionalized material 3 Wh dm^{-3} is thirty times that delivered by the non-functionalized sample 0.1 Wh dm^{-3} and even higher than that previously reported for phosphorus-functionalized activated carbons [17,48,49].

4. Conclusions

The synthesis temperature seems to play a crucial role in the control of the chemical state of the phosphorus-containing species; a large population of weakly bonded phosphate groups with C−O-P bonding are linked to the carbon matrix for the 400 °C treatment while more stable phosphates and phosphonate groups with C-*P = O* bonding also originates at 800 °C. Electrochemical response is optimum after phosphorus functionalization at 800 °C and phosphorus groups enlarge the potential stability window to 1.5 V. Apart from it, stable species clearly improve redox processes resulting in a gravimetric capacitance of 115 F g^{-1} and capacitance retention of 100% up to 100 mVs^{-1}. The charge storage in phosphorus-functionalized materials is influenced by both material composition and preliminary electrochemical cycling. It appears to involve multiple possible contributions: i) non-Faradaic charging; ii) nascent hydrogen storage; iii) benzoquinone-to-hydroquinone-like redox processes; iv) phosphate-to-phosphonate like transformation. Among these processes, prior electrochemical polarization to oxygen evolution potential is crucial at least in two respects: i) the emergence of redox reactions of quinones (otherwise undetected); ii) a significant improvement in the reversibly stored Faradaic charge below thermodynamic hydrogen evolution potential. In terms of performance, these findings translate into improvements in energy and power densities. The practical reversibility of the combined charge storage mechanisms is reflected in the excellent cycling stability upon 60,000 charge-discharge cycles.

Supplementary materials

Supplementary material associated with this article can be found, in the online version, at doi:10.1016/j.electacta.2020.136985.

References

[1] W. Raza, F. Ali, N. Raza, Y. Luo, K.-.H. Kim, J. Yang, S. Kumar, A. Mehmood, E.E. Kwon, Recent advancements in supercapacitor technology, Nano Energy 52 (2018) 441–473, doi:10.1016/j.nanoen.2018.08.013.

[2] A. González, E. Goikolea, J.A. Barrena, R. Mysyk, Review on supercapacitors: technologies and materials, Renew. Sustain. Energy Rev. 58 (2016) 1189–1206, doi:10.1016/j.rser.2015.12.249.

[3] J. Liu, J. Wang, C. Xu, H. Jiang, C. Li, L. Zhang, J. Lin, Z.X. Shen, Advanced Energy Storage Devices: basic Principles, Analytical Methods, and Rational Materials Design, Adv. Sci. 5 (2018) 1700322, doi:10.1002/advs.201700322.

[4] A.S. Lemine, M.M. Zagho, T.M. Altahtamouni, N. Bensalah, Graphene a promising electrode material for supercapacitors-A review, Int. J. Energy Res. 42 (2018) 4284–4300, doi:10.1002/er.4170.

[5] G. Zhang, Y. Han, C. Shao, N. Chen, G. Sun, X. Jin, J. Gao, B. Ji, H. Yang, L. Qu, Processing and manufacturing of graphene-based microsupercapacitors, Mater. Chem. Front. 2 (2018) 1750–1764, doi:10.1039/C8QM00270C.

[6] Y. Tao, X. Xie, W. Lv, D.-.M. Tang, D. Kong, Z. Huang, H. Nishihara, T. Ishii, B. Li, D. Golberg, F. Kang, T. Kyotani, Q.-.H. Yang, Towards ultrahigh volumetric capacitance: graphene derived highly dense but porous carbons for supercapacitors, Sci. Rep. 3 (2013), doi:10.1038/srep02975.

[7] L. Borchardt, M. Oschatz, S. Kaskel, Tailoring porosity in carbon materials for supercapacitor applications, Mater Horiz 1 (2014) 157–168, doi:10.1039/C3MH00112A.

[8] D. Salinas-Torres, R. Ruiz-Rosas, E. Morallón, D. Cazorla-Amorós, Strategies to Enhance the Performance of Electrochemical Capacitors Based on Carbon Materials, Front. Mater. 6 (2019), doi:10.3389/fmats.2019.00115.

[9] L. Hao, X. Li, L. Zhi, Carbonaceous Electrode Materials for Supercapacitors, Adv. Mater. 25 (2013) 3899–3904, doi:10.1002/adma.201301204.

[10] V... Strelko, V... Kuts, P... Thrower, On the mechanism of possible influence of heteroatoms of nitrogen, boron and phosphorus in a carbon matrix on the catalytic activity of carbons in electron transfer reactions, Carbon N Y 38 (2000) 1499–1503, doi:10.1016/S0008-6223(00)00121-4.

[11] Q. Abbas, R. Raza, I. Shabbir, A.G. Olabi, Heteroatom doped high porosity carbon nanomaterials as electrodes for energy storage in electrochemical capacitors: a review, J, Sci. Adv. Mater. Devices. 4 (2019) 341–352, doi:10.1016/j.jsamd.2019.07.007.

[12] D. Hulicova-Jurcakova, A.M. Puziy, O.I. Poddubnaya, F. Suárez-García, J.M.D. Tascón, G.Q. Lu, Highly Stable Performance of Supercapacitors from Phosphorus-Enriched Carbons, J. Am. Chem. Soc. 131 (2009) 5026–5027, doi:10.1021/ja809265m.

[13] D. Carriazo, M.C. Gutiérrez, F. Picó, J.M. Rojo, J.L.G. Fierro, M.L. Ferrer, F. del Monte, Phosphate-Functionalized Carbon Monoliths from Deep Eutectic Solvents and their Use as Monolithic Electrodes in Supercapacitors, ChemSusChem 5 (2012) 1405–1409, doi:10.1002/cssc.201200136.

[14] J. Patiño, N. López-Salas, M.C. Gutiérrez, D. Carriazo, M.L. Ferrer, F. del Monte, Phosphorus-doped carbon–carbon nanotube hierarchical monoliths as true three-dimensional electrodes in supercapacitor cells, J. Mater. Chem. A. 4 (2016) 1251–1263, doi:10.1039/C5TA09210H.

[15] C. Huang, T. Sun, D. Hulicova-Jurcakova, Wide Electrochemical Window of Supercapacitors from Coffee Bean-Derived Phosphorus-Rich Carbons, ChemSusChem 6 (2013) 2330–2339, doi:10.1002/cssc.201300457.

[16] N. Díez, C. Botas, E. Goikolea, D. Carriazo, Macroporous carbon monoliths derived from phloroglucinol–sucrose resins as binder-free thick electrodes for supercapacitors, J. Mater. Sci. 52 (2017) 11191–11200, doi:10.1007/s10853-017-0832-0.

[17] G. Moreno-Fernández, J.L. Gómez-Urbano, M. Enterría, T. Rojo, D. Carriazo, Flat-shaped carbon–graphene microcomposites as electrodes for high energy supercapacitors, J. Mater. Chem. A. 7 (2019) 14646–14655, doi:10.1039/C9TA03295A.

[18] P. Karthika, N. Rajalakshmi, K.S. Dhathathreyan, Phosphorus-Doped Exfoliated Graphene for Supercapacitor Electrodes, J. Nanosci. Nanotechnol. 13 (2013) 1746–1751, doi:10.1166/jnn.2013.7112.

[19] V. Thirumal, A. Pandurangan, R. Jayavel, K.S. Venkatesh, N.S. Palani, R. Ragavan, R. Ilangovan, Single pot electrochemical synthesis of functionalized and phosphorus doped graphene nanosheets for supercapacitor applications, J. Mater. Sci. Mater. Electron. 26 (2015) 6319–6328, doi:10.1007/s10854-015-3219-5.

[20] R. Berenguer, R. Ruiz-Rosas, A. Gallardo, D. Cazorla-Amorós, E. Morallón, H. Nishihara, T. Kyotani, J. Rodríguez-Mirasol, T. Cordero, Enhanced electrooxidation resistance of carbon electrodes induced by phosphorus surface groups, Carbon N Y 95 (2015) 681–689, doi:10.1016/j.carbon.2015.08.101.

[21] M.J. Valero-Romero, F.J. García-Mateos, J. Rodríguez-Mirasol, T. Cordero, Role of surface phosphorus complexes on the oxidation of porous carbons, Fuel Process. Technol. 157 (2017) 116–126, doi:10.1016/j.fuproc.2016.11.014.

[22] C. Wang, L. Sun, Y. Zhou, P. Wan, X. Zhang, J. Qiu, P/N co-doped microporous carbons from H3PO4-doped polyaniline by in situ activation for supercapacitors, Carbon N Y 59 (2013) 537–546, doi:10.1016/j.carbon.2013.03.052.

[23] C. Huang, A.M. Puziy, O.I. Poddubnaya, D. Hulicova-Jurcakova, M. Sobiesiak, B. Gawdzik, Phosphorus, nitrogen and oxygen co-doped polymer-based core-shell carbon sphere for high-performance hybrid supercapacitors, Electrochim. Acta 270 (2018) 339–351, doi:10.1016/j.electacta.2018.02.115.

[24] Y. Wen, B. Wang, C. Huang, L. Wang, D. Hulicova-Jurcakova, Synthesis of Phosphorus-Doped Graphene and its Wide Potential Window in Aqueous Supercapacitors, Chem. - Eur. J. 21 (2015) 80–85, doi:10.1002/chem.201404779.

[25] J.L. Gómez-Urbano, J.L. Gómez-Cámer, C. Botas, N. Díez, J.M. López del Amo, L.M. Rodríguez-Martinez, D. Carriazo, T. Rojo, Hydrothermally reduced graphene oxide for the effective wrapping of sulfur particles showing long term stability as electrodes for Li-S batteries, Carbon N Y 139 (2018) 226–233, doi:10.1016/j.carbon.2018.06.053.

[26] Y. Li, H. Chen, L.Y. Voo, J. Ji, G. Zhang, G. Zhang, F. Zhang, X. Fan, Synthesis of partially hydrogenated graphene and brominated graphene, J. Mater. Chem. 22 (2012) 15021, doi:10.1039/c2jm32307a.

[27] A.M. Puziy, O.I. Poddubnaya, R.P. Socha, J. Gurgul, M. Wisniewski, XPS and NMR studies of phosphoric acid activated carbons, Carbon N Y 46 (2008) 2113–2123, doi:10.1016/j.carbon.2008.09.010.

[28] B.J. Cade-Menun, C.R. Benitez-Nelson, P. Pellechia, A. Paytan, Refining 31P nuclear magnetic resonance spectroscopy for marine particulate samples: storage conditions and extraction recovery, Mar. Chem. 97 (2005) 293–306, doi:10.1016/j.marchem.2005.05.005.

[29] D. Hulicova-Jurcakova, M. Seredych, G.Q. Lu, N.K.A.C. Kodiweera, P.E. Stallworth, S. Greenbaum, T.J. Bandosz, Effect of surface phosphorus functionalities of activated carbons containing oxygen and nitrogen on electrochemical capacitance, Carbon N Y 47 (2009) 1576–1584, doi:10.1016/j.carbon.2009.02.006.

[30] V. Strelko Jr, M. Streat, O. Kozynchenko, Preparation, characterisation and sorptive properties of polymer based phosphorus-containing carbon, React. Funct. Polym. 41 (1999) 245–253, doi:10.1016/S1381-5148(99)00061-9.

[31] X. Liu, J. Li, X. Wang, C. Chen, X. Wang, High performance of phosphate-functionalized graphene oxide for the selective adsorption of U(VI) from acidic solution, J. Nucl. Mater. 466 (2015) 56–64, doi:10.1016/j.jnucmat.2015.07.027.

[32] X. Mu, B. Yuan, X. Feng, S. Qiu, L. Song, Y. Hu, The effect of doped heteroatoms (nitrogen, boron, phosphorus) on inhibition thermal oxidation of reduced graphene oxide, RSC Adv. 6 (2016) 105021–105029, doi:10.1039/C6RA21329D.

[33] M. Zakeri, E. Abouzari-lotf, M. Miyake, S. Mehdipour-Ataei, K. Shameli, Phosphoric acid functionalized graphene oxide: a highly dispersible carbon-based nanocatalyst for the green synthesis of bio-active pyrazoles, Arab. J. Chem. 12 (2019) 188–197, doi:10.1016/j.arabjc.2017.11.006.

[34] A. Kovtun, D. Jones, S. Dell'Elce, E. Treossi, A. Liscio, V. Palermo, Accurate chemical analysis of oxygenated graphene-based materials using X-ray photoelectron spectroscopy, Carbon N Y 143 (2019) 268–275, doi:10.1016/j.carbon.2018.11.012.

[35] R. Fu, L. Liu, W. Huang, P. Sun, Studies on the structure of activated carbon fibers activated by phosphoric acid, J. Appl. Polym. Sci. 87 (2003) 2253–2261, doi:10.1002/app.11607.

[36] Z. Bi, L. Huo, Q. Kong, F. Li, J. Chen, A. Ahmad, X. Wei, L. Xie, C.-.M. Chen, Structural Evolution of Phosphorus Species on Graphene with a Stabilized Electrochemical Interface, ACS Appl. Mater. Interfaces 11 (2019) 11421–11430, doi:10.1021/acsami.8b21903.

[37] M. Thommes, K. Kaneko, A.V. Neimark, J.P. Olivier, F. Rodriguez-Reinoso, J. Rouquerol, K.S.W. Sing, Physisorption of gases, with special reference to the evaluation of surface area and pore size distribution (IUPAC Technical Report), Pure Appl. Chem. 87 (2015) 1051–1069, doi:10.1515/pac-2014-1117.

[38] B. Lobato, R. Wendelbo, V. Barranco, T.A. Centeno, Graphite Oxide, An Interesting Candidate for Aqueous Supercapacitors, Electrochim. Acta 149 (2014) 245–251, doi:10.1016/j.electacta.2014.10.095.

[39] J. Piwek, A. Platek, K. Fic, E. Frackowiak, Carbon-based electrochemical capacitors with acetate aqueous electrolytes, Electrochim. Acta 215 (2016) 179–186, doi:10.1016/j.electacta.2016.08.061.

[40] A.A. El-Kady, H.H. Abdel Ghafar, M.B.M. Ibrahim, M.A. Abdel-Wahhab, Utilization of activated carbon prepared from agricultural waste for the removal of organophosphorous pesticide from aqueous media, Desalination Water Treat 51 (2013) 7276–7285, doi:10.1080/19443994.2013.792137.

[41] E. Goikolea, R. Mysyk, Chapter Four - Nanotechnology in Electrochemical Capacitors, in: L.M. Rodriguez-Martinez, N. Omar (Eds.), Emerg. Nanotechnologies Recharg. Energy Storage Syst., Elsevier, Boston, 2017, pp. 131–169, doi:10.1016/B978-0-323-42977-1.00004-2.

[42] C. Portet, P... Taberna, P. Simon, C. Laberty-Robert, Modification of Al current collector surface by sol–gel deposit for carbon–carbon supercapacitor applications, Electrochim. Acta 49 (2004) 905–912, doi:10.1016/j.electacta.2003.09.043.

[43] D. Weingarth, H. Noh, A. Foelske-Schmitz, A. Wokaun, R. Kötz, A reliable determination method of stability limits for electrochemical double layer capacitors, Electrochim. Acta 103 (2013) 119–124, doi:10.1016/j.electacta.2013.04.057.

[44] A.J. Bard, R. Parsons, J. JordanInternational Union of Pure and Applied Chemistry, Standard Potentials in Aqueous Solution, M. Dekker, New York, 1985 n.d..

[45] K. Jurewicz, E. Frackowiak, F. Béguin, Towards the mechanism of electrochemical hydrogen storage in nanostructured carbon materials, Appl. Phys. A. 78 (2004) 981–987, doi:10.1007/s00339-003-2418-8.

[46] J. Roels, W. Verstraete, Biological formation of volatile phosphorus compounds, Bioresour. Technol. 79 (2001) 243–250, doi:10.1016/S0960-8524(01)00032-3.

[47] C. Ma, Y. Song, J. Shi, D. Zhang, X. Zhai, M. Zhong, Q. Guo, L. Liu, Preparation and one-step activation of microporous carbon nanofibers for use as supercapacitor electrodes, Carbon N Y 51 (2013) 290–300, doi:10.1016/j.carbon.2012.08.056.

[48] Y. Wen, T.E. Rufford, D. Hulicova-Jurcakova, L. Wang, Nitrogen and Phosphorous Co-Doped Graphene Monolith for Supercapacitors, ChemSusChem 9 (2016) 513–520, doi:10.1002/cssc.201501303.

[49] A. Elmouwahidi, E. Bailón-García, A.F. Pérez-Cadenas, F.J. Maldonado-Hódar, F. Carrasco-Marín, Activated carbons from KOH and H 3 PO 4 -activation of olive residues and its application as supercapacitor electrodes, Electrochim. Acta 229 (2017) 219–228, doi:10.1016/j.electacta.2017.01.152.